Chapter 3

An analytical model for steady state atmospheric vortices: Application to dust devils

3.1 Introduction

Dust devils, also known as "miniature atmospheric vortices," are fascinating natural occurrences that appear in hot, dry, and still environments. Despite being challenging to study due to their transient nature, small spatial scale, and unpredictable occurrence, dust devils play a significant role in dust transport in arid environments, boundary layer processes, and vortex dynamics.

Among the earliest attempts to describe vortex-type phenomena was Rankine (1882) model, which provides a basic yet significant representation of a stationary vortex. This elementary model assumes the absence of radial and axial velocity components and simplifies the vortex into two distinct regions. These regions are divided by the radius

of maximum azimuthal velocity, denoted as r_c, where the azimuthal velocity reaches its peak value, V_m. In the core region, where $r < r_c$, the azimuthal velocity increases linearly with the radial distance and is expressed as $v = V_m r/r_c$. In the outer region, where $r \geq r_c$, the velocity decreases inversely with r and follows the relationship $v = V_m r_c/r$. Here, r represents the radial coordinate, r_c is the radius of maximum velocity, v denotes the azimuthal velocity, and V_m is the peak azimuthal velocity at $r = r_c$. This model captures the essential characteristics of a vortex by combining solid-body rotation in the core with potential flow behaviour in the outer region. Despite its simplicity, Rankine's vortex remains a foundational reference for understanding more complex vortex structures.

There are not many exact solutions available for the Navier-Stokes equations, which describe vortex structures. Few of them include the Sullivan (1959) and Burgers (1948) (or Burgers-Rott) vortices, Vatistas et al. (1991) and Wood and White (2011). The Burgers (1948) and Sullivan (1959) models describe 3-D axi-symmetric flows of viscous incompressible fluids. Burgers (1948) model describes viscous vortices by balancing vortex stretching and vorticity diffusion, but it becomes impractical at long radial distances because the radial and vertical velocities increase infinitely. A more realistic two-cell structure is introduced by the Sullivan (1959) vortex, where the outer cell has radial velocity inward and vertical velocity points upward, while the central cell has radial velocity outward and vertical velocity points downward. This model captures the interaction between radial and vertical flows, better simulating thermally driven vortices such as tornadoes and dust devils. Nevertheless, it also makes the idealised prediction that vertical velocity will increase indefinitely with height. Nevertheless, in atmospheric science, the Sullivan vortex is still a useful tool for comprehending convective vortex dynamics. A novel low-parametric model representing an exponentially localized vortex in space is presented in Onishchenko et al. (2021b). This model serves as an exact solution to the Euler equations for an incompressible fluid, which can also be viewed as a solution to the

inviscid form of the Navier-Stokes equations Onishchenko et al. (2018). Its inward radial flow concentrates vorticity into a narrow column centred around the axis of symmetry, much like the Burgers and Sullivan vortex. In contrast, the Batchelor (1964) vortex is an approximate solution to the Navier-Stokes equations, derived using boundary layer approximations that assume the axial gradients are insignificant in comparison to the radial gradients of flow. The axial velocity is controlled by vortex stretching and remains finite, while the radial velocity is zero $(u = 0)$, the azimuthal velocity increases linearly near the vortex core $(r \leq a)$, and decays inversely with radius outside the core $(r \geq a)$. A key limitation of the Batchelor vortex is that it has no radial flow and assumes steady-state conditions, which may not capture real-world unsteady or non-axisymmetric vortex dynamics. Despite these simplifications, the Batchelor vortex remains a fundamental model for studying trailing vortices, jet flows, and stability.

Vatistas et al. (1991) provide an empirical expression for the azimuthal velocity as a function of the radial distance r and the vortex core size a, with an adjustable shape parameter n controlling the velocity profile. While this model smoothly transitions between solid-body rotation near the vortex core and potential flow at larger radii, it assumes that the azimuthal velocity depends solely on the radial coordinate. This limitation means that the Vatistas model does not give the variations in axial or temporal directions, which makes it less suitable for capturing unsteady or three-dimensional vortex dynamics. In real-world vortices, azimuthal velocity often varies with axial position and time due to vortex stretching, boundary effects, or external forces, which the Vatistas model idealizes and simplifies. Wood and White (2011) and Wood et al. (2013) proposed a parametric azimuthal velocity profile by adopting and modifying the Vatistas et al. (1991) model. Wood and White (2011) gave a more general azimuthal profile that is dependent on both radial and axial coordinates but fails to include the vertical velocity.

Both theoretical and numerical methods have been used to study the formation,

behaviour, and interactions of dust devils with their surroundings. Early work includes studies by Sinclair (1973), who investigated the lower structure of dust devils, and Smith and Leslie (1976), who conducted numerical studies on thermally driven vortices, applying their findings to dust devil dynamics. Other developments include Toigo et al. (2003) simulated Martian dust devils and Pandey and Yadav (2024) gave mathematical model of tropical cyclone focussing on impact of eye-size on intensification of cyclone. Onishchenko et al. (2018, 2019, 2021b) introduced models of quasi-stationary vortices that explored structural features, dynamics, and their role in unstable stratified atmospheres. Farrell et al. (2003a) discovered that dust devils are not only shaped by hydrodynamic forces, but also by electromagnetic forces. He integrated electrostatic and fluid dynamics to explain dust devil electric and magnetic signatures (Farrell et al. (2003a) Farrell et al. (2004) Farrell et al. (2006)). Laboratory experiments further validated these findings, with Melnik and Parrot (1998) identifying electrostatic discharge in dust storms, while Zhou et al. (2002) and Zheng et al. (2003) measured sand flux, transport dynamics, and electrification effects through wind-blown sand experiments. Pandey and Maurya (2018a) presented an exact solution for the unsteady flow of atmospheric vortices, an extension of Burgers (1948) model. There are a few more analytical models describing various features available in the literature (Sinclair (1965), Horton et al. (2016), Kolomenskiy and Moffatt (2012), Moffatt (2000), Onishchenko et al. (2014b), Rotunno (2013), Yadav et al. (2024)).

Vyas and Majdalani (2006) reported an exact solution to the bidirectional vortex flow, who assumed that the azimuthal velocity is solely dependent on the radial coordinate. It is an inverse relationship between azimuthal velocity and radial coordinate. While this assumption simplifies the analysis, it does not account for variations in the axial direction, which are significant in real-world vortex structures (Vyas and Majdalani (2007); Majdalani and Chiaverini (2002)). Motivated by the need for a more general and comprehensive vortex model, this attempt aims to extend the analysis by incorporating axial

dependence of the velocity field. A generalized form of the velocity components, dependent on both radial and axial coordinates, is derived.

3.2 Mathematical formulation of the problem

3.2.1 Physical Model

Dust devils are usually found in arid areas, forming due to the strong temperature gradient caused by intense heating of the ground. This gradient causes air near the surface to rise, which creates a low-pressure cylindrical zone, and to maintain the equilibrium, cooler winds from all directions rush towards the low-pressure zone, which sometimes generates a rotating column of air. These swirling columns of air mixed with dust particles ascend into the sky and dissipate quickly.

3.2.2 Mathematical model

We consider the cylindrical polar coordinate system ($\tilde{r}$, $\tilde{\theta}, \tilde{z}$) to analyse the dynamics. The shape of the dust devil is assumed to be a cylinder. Empirical observations suggest consistency in the behaviour of a rotating fluid mass configured as a vortex, regardless of its angular orientation during vertical axis rotation. As a result, we consider the flow pattern to exhibit axial symmetry. The three-dimensional Navier-Stokes equations for the steady axi-symmetric flow of an incompressible Newtonian inviscid fluid be given by

$$\left(\tilde{u}\frac{\partial \tilde{u}}{\partial \tilde{r}} + \tilde{w}\frac{\partial \tilde{u}}{\partial \tilde{z}} - \frac{\tilde{v}^2}{\tilde{r}}\right) = -\frac{1}{\rho}\frac{\partial \tilde{p}}{\partial \tilde{r}} \qquad \text{(Radial Momentum)} \tag{3.1}$$

$$\left(\tilde{u}\frac{\partial \tilde{v}}{\partial \tilde{r}} + \tilde{w}\frac{\partial \tilde{v}}{\partial \tilde{z}} + \frac{\tilde{u}\tilde{v}}{\tilde{r}}\right) = 0 \qquad \text{(Azimuthal Momentum)} \tag{3.2}$$

$$\left(\tilde{u}\frac{\partial \tilde{w}}{\partial \tilde{r}} + \tilde{w}\frac{\partial \tilde{w}}{\partial \tilde{z}}\right) = -\frac{1}{\rho}\frac{\partial \tilde{p}}{\partial \tilde{z}} \qquad \text{(Vertical Momentum)} \tag{3.3}$$

$$\frac{1}{\tilde{r}}\frac{\partial(\tilde{r}\tilde{u})}{\partial \tilde{r}} + \frac{\partial \tilde{w}}{\partial \tilde{z}} = 0 \qquad \text{(Continuity)} \tag{3.4}$$

where $\tilde{u}$, $\tilde{v}$, $\tilde{w}$ denote the velocity component of fluid motion in the $\tilde{r}$-, $\tilde{\theta}$-, $\tilde{z}$- directions while $\tilde{p}$ being pressure, ρ symbolizing density.

3.3 Normalization

To achieve dynamical similarity, we non-dimensionalise the governing equations (3.1–3.4) by introducing the following dimensionless variables

$$r = \frac{\tilde{r}}{r_m}, z = \frac{\tilde{z}}{L}, u = \frac{\tilde{u}}{v_m}\ v = \frac{\tilde{v}}{v_m}, w = \frac{\tilde{w}}{v_m}, p = \frac{\tilde{p}}{\rho v_m^2},$$

v_m being the maximum azimuthal velocity, r_m the characteristic radius and L the characteristic axial length. In this article, we work on the inviscid and incompressible flow, hereby, the decomposed equations are

$$u\frac{\partial u}{\partial r} + \lambda w\frac{\partial u}{\partial z} - \frac{v^2}{r} = -\frac{\partial p}{\partial r}, \tag{3.5}$$

$$u\frac{\partial v}{\partial r} + \lambda w\frac{\partial v}{\partial z} + \frac{uv}{r} = 0, \tag{3.6}$$

$$u\frac{\partial w}{\partial r} + \lambda w\frac{\partial w}{\partial z} = -\lambda\frac{\partial p}{\partial z}, \tag{3.7}$$

$$\frac{1}{r}\frac{\partial}{\partial r}(ru) + \lambda\frac{\partial w}{\partial z} = 0, \tag{3.8}$$

where $\lambda = r_m/L$ is aspect ratio.

3.4 Solution

In this work, we present a modified stream function for incompressible axisymmetric flow in cylindrical coordinates. Building upon the formulation by Vyas and Majdalani (2006), where $\psi = Cz\sin(\pi r^2)$ and C is a constant, we incorporate an exponential decay term e^{-z} to introduce axial dependence in the velocity field. Unlike the original model, where the radial and azimuthal velocities are solely functions of the radial coordinate, the proposed stream function ensures that all velocity components depend on both r and z. The radial behaviour is preserved through the $\sin(\pi r^2)$ term, while the added axial modulation offers a more realistic and physically consistent representation of vortex flows with vertical structure. The resulting modified stream function is

$$\psi = Cze^{-z}sin(\pi r^2). \tag{3.9}$$

The presence of e^{-z} causes ψ reduce to zero as $z \to \infty$. Further using the Stokes stream-function ψ, we determine the velocity components in the radial and vertical directions through

$$u = -\lambda\frac{1}{r}\frac{\partial\psi}{\partial z} \quad \text{and} \quad w = \frac{1}{r}\frac{\partial\psi}{\partial r}. \tag{3.10}$$

Substituting ψ in Eq. (3.10), we can derive the velocity components

$$u = -C\lambda\frac{sin(\pi r^2)}{r}(1-z)e^{-z}, \tag{3.11}$$

$$w = 2C\pi zcos(\pi r^2)e^{-z}. \tag{3.12}$$

For evaluating the value of C, we use the global mass balance condition (Vyas and Majdalani (2006),

$$2\pi \int_0^{r_m} w(r, L) r \, dr = Q_i, \tag{3.13}$$

$$C = \frac{Q_i}{2\pi L e^{-L} sin(\pi r_m^2)} = \frac{1}{2\sigma\pi L e^{-L} sin(\pi r_m^2)}, \tag{3.14}$$

where $Q_i^{-1} = \sigma$ and Q_i, σ stands for volumetric flow rate and modified swirl number respectively. A larger C corresponds to stronger inflow and upward motion, indicating more vigorous convective activity in the vortex.

3.4.1 Azimuthal velocity

The azimuthal component of the momentum equation in steady, inviscid, axi-symmetric flow is

$$u\frac{\partial v}{\partial r} + \lambda w \frac{\partial v}{\partial z} + \frac{uv}{r} = 0, \tag{3.15}$$

which we write in characteristic form

$$\frac{dr}{u} = \frac{dz}{\lambda w} = \frac{dv}{-\frac{uw}{r}}. \tag{3.16}$$

The resulting azimuthal velocity is obtained

$$v = Cze^{-z}\frac{sin(\pi r^2)}{r}. \tag{3.17}$$

The details of the calculations are presented in Appendix.

3.4.2 Pressure

Using Eq. (3.5), the radial pressure gradient is derived as follows

$$
\begin{aligned}
-\frac{\partial p}{\partial r} = C^2\lambda^2(1-z)^2e^{-2z}&\left(\frac{\pi r^2\sin\left(2\pi r^2\right)-\sin^2\left(\pi r^2\right)}{r^3}\right)\\
&+2C^2\lambda^2\pi z(z-2)e^{-2z}\cdot\frac{\sin\left(\pi r^2\right)\cos\left(\pi r^2\right)}{r}\\
&-C^2z^2e^{-2z}\cdot\frac{\sin^2\left(\pi r^2\right)}{r^3}.
\end{aligned}
\tag{3.18}
$$

Integrating this expression yields

$$
\begin{aligned}
p(r,z) = p(0,z) - \int_0^r\Bigg[&C^2\lambda^2(1-z)^2e^{-2z}\left(\frac{\pi s^2\sin\left(2\pi s^2\right)-\sin^2\left(\pi s^2\right)}{s^3}\right)\\
&+2C^2\lambda^2\pi z(z-2)e^{-2z}\cdot\frac{\sin\left(\pi s^2\right)\cos\left(\pi s^2\right)}{s}\\
&-C^2z^2e^{-2z}\cdot\frac{\sin^2\left(\pi s^2\right)}{s^3}\Bigg]ds.
\end{aligned}
\tag{3.19}
$$

This integral is evaluated numerically to obtain the pressure distribution as a function of radial distance r at different heights z.

3.5 Results and Discussion

3.5.1 Streamlines

Streamlines of the flow field are plotted in r-z plane in Fig. (3.1). The contours show a consistent vortex-like pattern, suggesting continuous and smooth velocity components. The streamlines converge, indicating a steep axial gradient near the central region of the vortex. This suggests a rapid increase in axial velocity as the flow progresses upward.

As r gets closer to zero, the radial velocity decreases, forming a near-axis stagnation area that makes it easier for lighter particles to be lifted. An acceleration of the axial velocity, which is essential for the vertical elongation of dust devil, is shown by the denser streamlines in the centre of the vortex. The streamlines become more dispersed at larger radial distances, demonstrating a gradual decrease in the axial velocity magnitude. This depicts the weakening of the flow field as the distance from the axis increases.

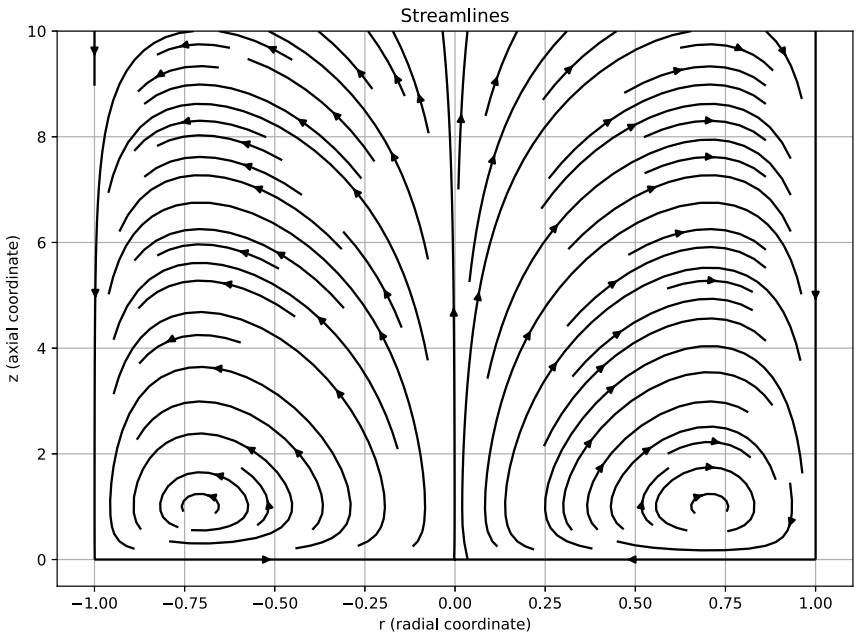

Figure 3.1: Streamlines of u and w along radial r and axial axis z

3.5.2 Radial Velocity Distribution

The radial component of velocity is deduced from the formula given by Eq. (3.11). The corresponding radial velocity profile is depicted in Fig. (3.2). For lower altitudes ($z < 1$), as shown in Fig. (3.2a), the profile shows a substantial increase in the absolute magnitude of radial velocity towards the central region of the vortex. Further, it undergoes a gradual decrease, ultimately diminishing to zero as it approaches the axis. For heights above $z = 1$, an outflow is observed. In the range $1 < z < 2$ shown in Fig. (3.2b), the radial velocity

increases with height across the curves, while it decreases for $z > 2$, compatible with the formula in Eq. (3.11) (Fig. (3.2c)).

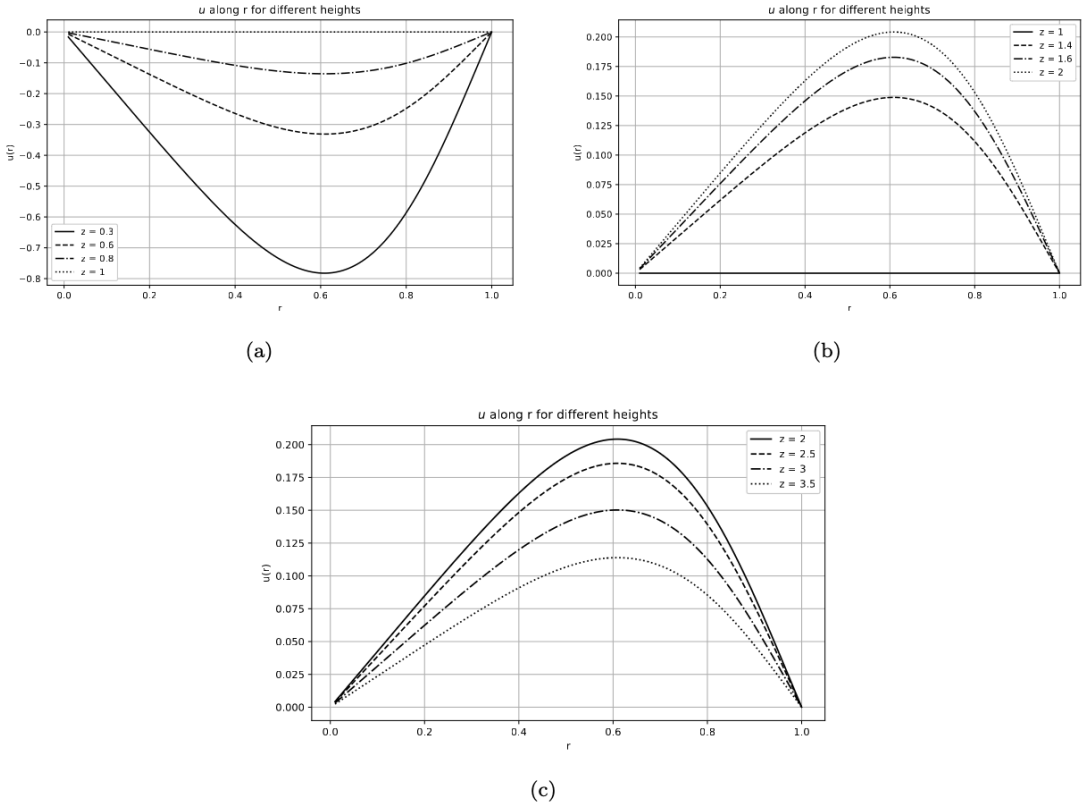

Figure 3.2: Plots (a)-(c) represent the radial profile of the non-dimensionalised radial velocity for $z \leq 1$, $1 \leq z \leq 2$ and $z \geq 2$ respectively.

3.5.3 Axial Velocity Distribution

Fig. (3.3) presents the radial profiles of the derived vertical velocity given in Eq. (3.12) for different altitudes. It is observed that the winds rise faster as they come closer to the vertical axis, and also at higher altitudes, the wind velocity increases to reach a maximum at $r = 0$. Axial velocity exhibits a distinct pattern characterized by negative values beyond the confines of the vortex. The boundary of the updraft region is marked by zero axial velocity beyond which it is negative, paving the way for the dust particles to settle down

on the ground. It is theoretically estimated and also graphically observed that the axial velocity is zero at $r \approx 0.707$. In Fig. (3.3a), the vertical velocity intensifies with height for $0 < z < 1$, whereas in Fig. (3.3b) it weakens as z increases.

Practically, the dust particles are not expected to get grounded with the observed velocity due to the presence of buoyancy; they would rather fall very slowly, get scattered in the atmosphere.

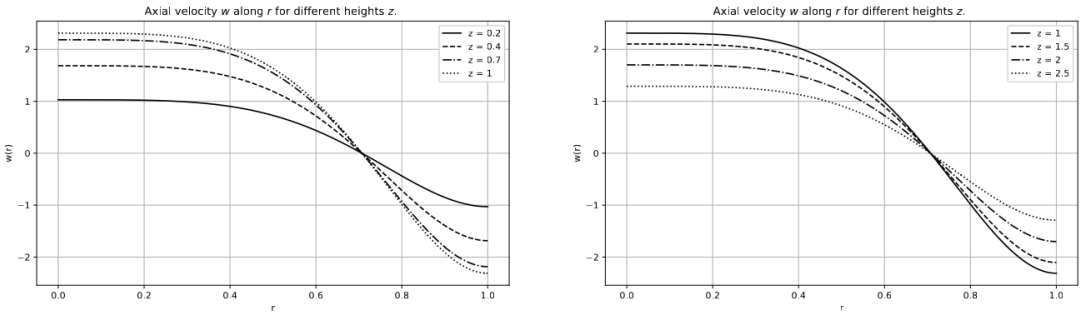

(a) (b)

Figure 3.3: Plots (a) and (b) represent the radial profile of the non-dimensionalised axial velocity for $z \leq 1$ and $z > 1$, respectively.

3.5.4 Azimuthal Velocity Distribution

Azimuthal velocity characterizes vortex motion. It emerges as the primary velocity component of interest. It is computed by using radial and axial components of velocity into $\theta-$ momentum equation, formulated in Eq. (3.19). Fig. (3.4) demonstrates the radial profile of azimuthal velocity. It exhibits an incremental rise from the vortex's centre towards the periphery, where it attains its maximum magnitude. Subsequently, azimuthal velocity undergoes a gradual decline, ultimately dissipating to zero. Refan et al. (2017) gave a velocity profile analysis using the ground-based velocity track display method on Doppler radar data on tornadoes. They simulated the collected data for different heights

against Rankine and modified Rankine models. However, the radial profiles of the azimuthal velocity given by Refan et al. (2017) are in good agreement with those of this model.

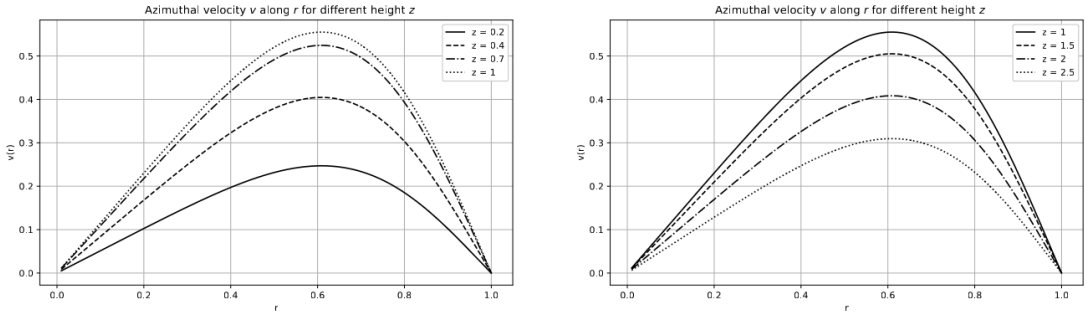

(a) (b)

Figure 3.4: Plots (a) and (b) represent the normalized azimuthal velocity along radial distance for $z \leq 1$ and $z > 1$, respectively.

Fig. (3.5) illustrate a comparative study of the azimuthal velocity profiles for several classical vortex models such as the Rankine (1882), Burgers (1948), Vatistas et al. (1991) (with $n = 2$), Sullivan (1959), and the present model. The Rankine vortex exhibits a linear increase in velocity within the core, followed by an abrupt $1/r$ decay, resulting in a discontinuous vorticity distribution. In contrast, the Burgers model provides a smooth transition, rising linearly near the centre and decaying asymptotically with $1/r$, capturing viscous effects. The Vatistas model generalizes this behaviour by introducing a shape parameter n, allowing flexible profile tuning. The Sullivan model presents a decaying exponential form suitable for near-surface vortex flows. In comparison, the present model features a smoothly increasing and then decaying profile. Unlike the classical models, it confines the flow within a finite domain, ensures smoothness at both $r = 0$ and $r = 1$, and introduces vertical dependence through z. Additionally, its growth near the core is slower than linear, representing a weak-core structure observed in dust devils. Overall, the present model provides a physically consistent and compact model, capturing both the rotational and vertical structure of dust devils with high smoothness and bounded behaviour. Fig.

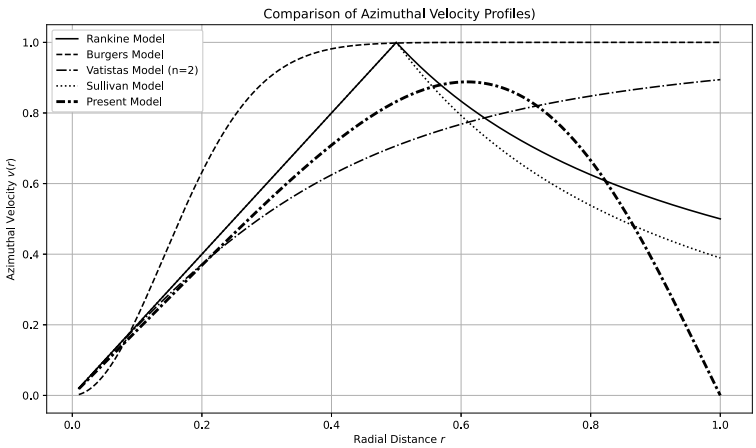

Figure 3.5: Comparison of azimuthal velocity profiles for different vortex models: Rankine, Burgers, Vatistas ($n = 2$), Sullivan, and the present model. The present model exhibits a bounded and smooth structure, peaking near $r \approx 0.6$, and introduces vertical variation through z.

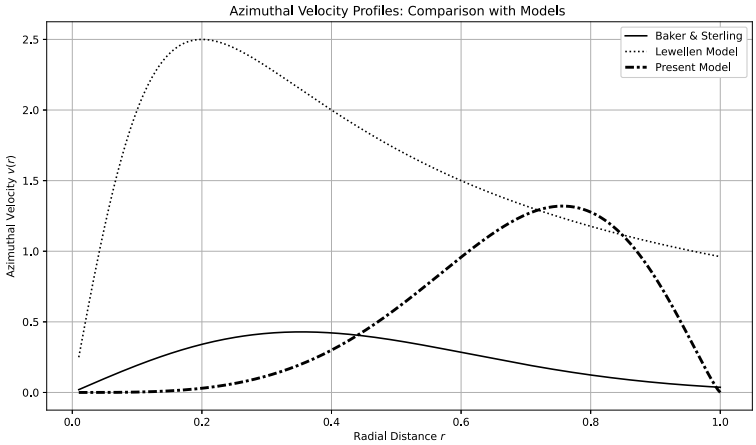

Figure 3.6: Azimuthal velocity profiles compared across the Baker and Sterling model, Lewellen model, and the present analytical model.

(3.6) compares the present model with two other vortex representations based on numerical simulation and laboratory observations, the Baker and Sterling (2017) and the Lewellen et al. (1997). The Baker and Sterling profile exhibits a broad and gentle peak closer to the centre of the vortex, representing a relatively diffused vortex core, whereas the Lewellen model demonstrates a sharper peak and a more rapid decay, indicative of a strong central rotation and higher vorticity near the core. In contrast, the present model features a distinct

structure with peak azimuthal velocity farther from the centre of the vortex compared with the other two, offering a more compact and bounded rotational profile. While the classical models decay gradually and extend to larger radii, the present model is confined within a finite domain and introduces vertical dependence through the z parameter. This reflects more localized vortex structures typical of dust devils, where the rotation is confined and smoothly transitions to quiescent air at the periphery.

3.5.5 Pressure Distribution

Radial pressure plays a vital role in the formation of dust devils. Its radial distribution is presented in Fig. (3.7) based on Eq. (3.19). Obviously, on the outer boundary of the dust devil, radial pressure is maximum but diminishes gradually as it reaches the centre. This is supported by the steep fall of pressure close to the centre of the vortex. The curves corresponding to various altitudes show a slight decrease at lower altitudes, noticed away from the centre of the vortex, and become constant for higher altitudes, in contrast to earlier reports on radial pressure.

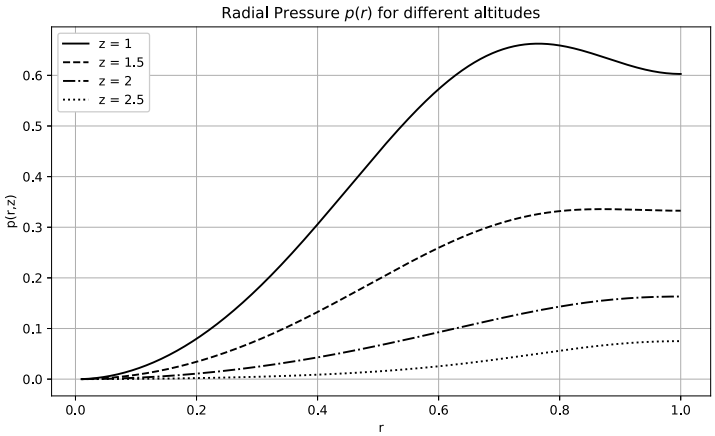

Figure 3.7: Pressure distribution

3.5.6 Implications for Saltation and Electrification

The vortex structure developed in this work not only models dust devil circulation but also offers an understanding of electrical charging mechanisms and particle lifting. Predicted converging radial inflow and strong updraft near the core ($r \approx 0.7$) produce increased surface shear stress and pressure deficits, enabling saltation by exceeding threshold friction velocities. Lifted particles are entrained into the updraft once started, so creating the dust column. Fig. (3.8) shows the schematic vertical distribution of electric charge inside a dust devil vortex. While a high concentration of negative charges accumulates aloft, separated by an intermediate mixed-charge zone that generates strong vertical electric fields, positive surface charges dominate near the ground.

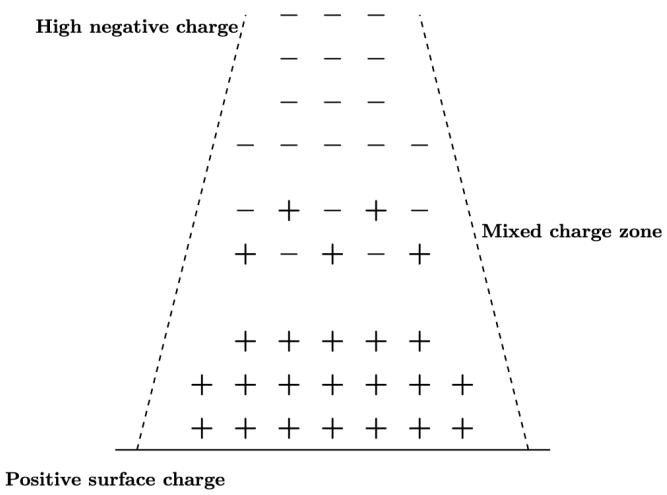

Figure 3.8: Schematic of vertical charge distribution in a dust devil vortex.

The model's axial dependence in the azimuthal velocity promotes vertical particle segregation, favouring triboelectric charge separation, as observed in laboratory studies Zhou et al. (2002); Zheng et al. (2003). Our results indicate that regions of maximum vertical velocity align with zones of strongest particle acceleration and probable electrification, consistent with field measurements Farrell et al. (2003b). Furthermore, the vortex

confinement within a finite radius suggests that dust devils modelled here act as localized sources of atmospheric dust and electrostatic enhancement.

3.6 Conclusion

The modified stream function is in conformity with the reported experimental results/-data. At an infinite distance from the axis, it is zero, indicating an absence of velocity. The modification brings about desired improvements in velocity components given in the subsequent paragraphs.

At lower altitudes ($z < 1$), the radial velocity profiles exhibit an increase in the absolute magnitude towards the central region of the vortex. Further, radial velocity decreases and eventually gets eliminated near the axis. For heights above $z = 1$, an outflow is observed. However, radial velocity increases vertically with height in the range $0 < z < 2$ but weakens above $z > 2$.

The axial velocity profiles exhibit realistic updraft patterns centred along the axis, while the radial velocity smoothly declines toward the core. Vertical velocity increases with height in the range $0 \leq z \leq 1$ but decreases beyond. Axial velocity is zero at $r = 1/\sqrt{2}$.

This model confirms a finite width of dust devils as the azimuthal velocity vanishes at a finite distance from the axis. The azimuthal component is, however, strongest at $r \approx 0.776$ and decreases on both sides to ultimately disappear at the central axis and also at a finite distance from it.

The pressure distribution captures the low-pressure zone at the vortex centre, aligning with atmospheric vortex dynamics.

Compared with traditional models such as Burgers and Rankine vortices, the present formulation better captures the confined, vertically evolving structure characteristic of dust devils. Moreover, the analytical expressions provide feasible answers for the investigation of localised dust movement, electrification, and saltation.

The generalized framework presented here offers a significant step towards modelling atmospheric vortices on a small scale in a more realistic manner.

Appendix A

The azimuthal component of the momentum equation in steady, inviscid, axi-symmetric flow is

$$u\frac{\partial v}{\partial r} + w\lambda\frac{\partial v}{\partial z} + \frac{uv}{r} = 0, \tag{3.A.1}$$

which we write in characteristic form

$$\frac{dr}{u} = \frac{dz}{\lambda w} = \frac{dv}{-\frac{uv}{r}}. \tag{3.A.2}$$

This implies a set of equations describing the evolution of the flow along streamlines. From the first two terms, we get

$$\frac{dr}{dz} = \frac{u}{\lambda w}, \quad \text{or} \quad u = \frac{dr}{dz}\cdot\lambda w, \tag{3.A.3}$$

from and second and third,

$$\frac{dv}{dz} = -\frac{uv}{\lambda r w} \tag{3.A.4}$$

Using Eq.(3.A.3) in Eq.(3.A.4), we get

$$\frac{dv}{dz} = -\frac{v}{r}\cdot\frac{dr}{dz} \quad \text{or} \quad \frac{dv}{v} = -\frac{dr}{r}, \tag{3.A.5}$$

integrating which we obtain

$$\ln v = -\ln r + \ln \beta, \quad \beta \text{ being constant, i.e., } \quad v(r,z) = \frac{\beta}{r}. \tag{3.A.6}$$

Assuming conservation of angular momentum in axisymmetric inviscid flow, we conclude $rv =$ constant along streamlines, which implies

$$rv = f(\psi) \quad \text{or} \quad v = \frac{f(\psi)}{r}. \tag{3.A.7}$$

Taking the simplest form of $f(\psi)$, azimuthal velocity may be given by

$$v(r,z) = Cze^{-z}\frac{sin(\pi r^2)}{r}. \tag{3.A.8}$$

****